Pergamon

Geochimica et Cosmochimica Acta, Vol. 67, No. 13, pp. 2427–2441, 2003

0016-7037/03 $30.00 + .00

doi:10.1016/S0016-7037(00)01407-2

Rate of hydrogen–iron redox exchange in silicate melts and glasses

FABRICE GAILLARD,* BURKHARD SCHMIDT, STEVEN MACKWELL, and CATHERINE MCCAMMON
Bayerisches Geoinstitut, Universität Bayreuth, D-95440 Bayreuth, Germany

(*Received July* 30, 2002; *accepted in revised form December* 9, 2002)

Abstract—A kinetic model for the rate of iron–hydrogen redox exchange in silicate glasses and melts has been derived from time-series experiments performed on natural rhyolitic obsidians. Cylinders of the starting glasses were exposed to reducing mixtures composed of H_2-Ar-CO_2-CO in 1-atm furnaces and H_2-Ar in a cold seal pressure vessel. Overall, runs covered the temperature range 300 to 1000°C. The progression of a front of ferric iron reduction within the quenched melt was observed optically through a change of color. For all run conditions, the advancement of the front (ξ) was proportional to the square root of time, revealing the reaction as a diffusion-limited process. Iso-fO_2 runs performed in CO_2-CO, H_2-Ar, and H_2-CO_2 gases have shown that fH_2 rather than fO_2 is the dominant parameter controlling the reaction rate. The fH_2 dependence of the rate constant was characterized in the range 0.02 to 70 bar. The growth of the reduced layer, which is accompanied by an increase in reaction-derived OH-group content, was fitted considering that the reaction rate is controlled by the migration of a free mobile species (H_2) immobilized in the form of OH subsequent to reaction with ferric iron. The reaction rate is thus a function of both solubility and diffusivity of H_2 weighted by the concentration of its sink (ferric iron). We extracted a single law for both solubility and diffusivity of H_2 in amorphous silicates that applies over a range of temperatures below and above the glass transition temperature. Melt/glass structure (degree of polymerization) does not seem to significantly affect both solubility and diffusivity of H_2. We therefore provide a model that allows the prediction of oxidation–reduction rates in the presence of hydrogen for a wide range of compositions of amorphous glasses and melts. Comparisons with previous work elucidating rate of redox exchange in dry systems allow us to anticipate the fH_2-T domains where different redox mechanisms may apply. We conclude that equilibration of redox potential in nature should be dominated by H_2 transfer at a rate controlled by both H_2 solubility and diffusion. Numerical applications of the model illustrate redox exchanges in natural magmas and in glasses exposed to weathering under near surface conditions. We show that crustal events such as magmas mixing should not modify the iron redox state of magmas. In the case of nuclear-waste-bearing glasses, the fH_2 conditions in the host terrain are clearly a parameter that must be taken into account to predict glass durability.

1. INTRODUCTION

The redox ratio of multivalent elements in amorphous silicates is known to affect properties such as color, viscosity, structure, and crystal–liquid equilibria (Osborn, 1959; Mysen et al., 1985; Dingwell, 1994; Martel et al., 1999). For example, many studies have focused on the redox state of iron in silicate melts because iron is the most abundant multivalent element in natural glasses (Kress and Carmichael, 1991; Gaillard et al., 2001). Nevertheless, the question of the mechanisms of redox potential communication in amorphous silicates has only recently been evaluated (Cooper et al., 1996; Cook and Cooper, 2000). Cooper and coworkers have articulated an elegant kinetic model clarifying the rate and mechanisms of iron oxidation and reduction in anhydrous silicate glasses and melts. However, the applicability of this model to processes operating on and within the Earth may be questionable because water is ubiquitous from the surface to several hundreds of kilometers of depth (Johnson et al., 1994; Ingrin and Skogby, 2000; Bolfan-Casanova et al., 2002; Pichavant et al., 2002). Gaillard and coworkers (see Gaillard et al., 2002, 2003) have recently demonstrated that under both water-rich and water-poor conditions the kinetic model of Cooper and coworkers does not operate; instead, the couple H_2/H_2O dominates the redox behavior of melts and imposes reaction rates much faster than under anhydrous conditions. It follows that the current models do not allow the rate of redox exchange between amorphous silicates and their surroundings to be properly predicted. For example, although the terrestrial magma redox state is very heterogeneous (Carmichael, 1991), the mechanisms of acquisition of this redox signature, and therefore its origin, remain unconstrained. With respect to processes close to the Earth's surface, mechanisms of redox alteration of glasses under wet conditions are unclear, although the durability of waste-bearing glasses may depend on it. This article provides a kinetic model for the rate of iron–hydrogen redox exchange in silicate glass–melt that has been derived from time-series experiments performed on natural rhyolitic obsidians. Applications relevant to natural redox alterations of magmas and waste-bearing glasses are proposed. In particular, we show that redox alteration of glasses under low-temperature conditions may lead to irreversible hydration of the glass at a rate much greater than water diffusion, which should have crucial implications in terms of durability of waste-bearing glasses.

2. BACKGROUND AND STARTING HYPOTHESES

The redox state of a melt or glass, described here by the ferric/ferrous ratio is commonly related to the prevailing oxygen fugacity, fO_2:

* Author to whom correspondence should be addressed (fabrice.gaillard@uni-bayreuth.de).

Table 1. Composition of the starting obsidian.[a]

SiO_2	TiO_2	Al_2O_3	MgO	FeO	CaO	Na_2O	K_2O	OH[b]	Fe^{3+}/Fe^{tot} [c]
74.51	0.10	13.25	0.08	1.60	0.75	4.15	5.64	0.125	0.2
0.55	0.06	0.12	0.05	0.08	0.04	0.06	0.10	0.004	0.05

[a] Number in weight % except Fe^{3+}/Fe^{tot}, expressed in atoms. First row is composition and second is standard deviation or uncertainty.
[b] Obtained from FTIR; see part 3.
[c] Obtained from Mossbauer spectroscopy.

$$FeO + \tfrac{1}{4}O_2 \Leftrightarrow FeO_{1.5} \quad (1)$$

Natural magmas in the Earth's interior display an fO_2 generally much lower than 10^{-6} bar, and therefore they do not contain significant amounts of molecular O_2. Oxygen fugacity therefore has thermodynamic implications relating the ferric–ferrous ratio of a melt to a value of fO_2 (see Kress and Carmichael, 1991). However, it is fundamental to understand that Eqn. 1 describes an equilibrium and not a reaction. It follows that Eqn. 1 does not account for the actual reaction path operating during changes of iron redox state in the melt. The reaction path involves the most abundant species having the greatest ability to dissipate the redox disequilibria. According to Cooper and coworkers (Cooper et al., 1996; Cook and Cooper, 2000), iron oxidation–reduction in dry silicate melts is rate controlled by migration of divalent cations (Ca^{2+}, Mg^{2+}, Fe^{2+}). In such dry melts, O^{2-}/O_2 and Fe^{2+}/Fe^{3+} are the dominant redox couples. However, because of the sluggish mobility of both O^{2-} and O_2 in the investigated liquids, oxidation occurs by outward removal of cations rather than inward incorporation of O^{2-} or O_2. The result, in the case of oxidation, is an increased ratio of the oxygen anions over cations. In water-bearing melts, H_2/H_2O and Fe^{2+}/Fe^{3+} are the dominant redox couples. In such melts, Gaillard and coworkers (Gaillard et al., 2002, 2003) have shown that migration of divalent cations does not operate during oxidation and reduction of iron. Rather, iron oxidation and reduction operate respectively through extraction and incorporation of hydrogen under the form H_2 or H^+. Gaillard and coworkers noticed a delay of oxidation and reduction relative to H_2 velocity in the melt. To explain this delay, Gaillard et al. (2002) suggested that iron oxidation reduction is a reaction-limited process in which H_2 diffusion (DH_2) is not rate limiting. More recently, this hypothesis was partly dismissed because coupled iron reduction and hydrogen incorporation was established as a diffusion-limited process (Gaillard et al., 2003). The suggested reaction was written as (Hess' notations; Hess, 1980)

$$H_2 + 2\,NaFe^{3+}O_2 + 2\,SiOSi \Leftrightarrow 2\,NaOH + 4\,(Fe^{2+})_{0.5}OSi \quad (2)$$

At 800°C, molecular H_2 was revealed to be a very mobile species ($DH_2 \sim 10^{-8}$ $m^2 \cdot s^{-1}$) in comparison to the relatively slow progression rate of reaction 2 ($\sim 10^{-11}$ $m^2 \cdot s^{-1}$). The authors proposed that coupled electron–proton mobilities within the melt may control the reaction rate and/or the latter may be slowed down by a low supply of molecular H_2 at the reaction front. The problem can be described as diffusion of a free component (H_2) reacting with the melt. The reaction products therefore may or may not be mobile species (e^- and H^+).

In the scenario where molecular H_2 is the only mobile species (and is therefore rate controlling), the delay between DH_2 and the rate of iron oxidation–reduction could be explained by a very low H_2 solubility (S_{H_2}) in the melt in comparison with the amount of ferric iron (X_{Fe}^{3+}) (i.e., the ratio $S_{H_2}/X_{Fe}^{3+} \ll 1$). As the H_2 solubility in the melt is a function of fH_2, the reduction rate of iron should be, in part, controlled by the fH_2. The temperature dependence of the redox reaction should correspond to the activation energy of H_2 diffusion. We present experiments on the effect of H_2 fugacity and temperature on the rate of iron oxidation–reduction with the aim of elucidating the involved mechanisms. We demonstrate that the reaction rate and the associated mechanisms can be interpreted in terms of dissolution + diffusion + immobilization (i.e., reaction) of the H_2 species in the melt, where the diffusion step is rate limiting.

3. STRATEGY AND TECHNICAL DETAILS

A natural metaluminous obsidian containing less than 3% volume of crystalline material was used as a starting material for all experiments. This obsidian is bubble-free. A few grains of magnetite ($\sim$1 to 10 μm) were observed and characterized by scanning electron microscopy but were so sparse that their contribution to the bulk ferric–ferrous ratio of the sample was negligible. The chemical composition (major elements), water content, and relative proportion of ferric and ferrous iron are given in Table 1. We estimated the glass transition temperature of this obsidian to be $\sim$850°C (see below).

Experiments consisted of exposing cylinders of the starting obsidian to reduced gas mixtures with which it was not in equilibrium. Cylinders sizes were always 4 mm in diameter. By performing time-series runs, the reaction advancement was monitored as a function of time. Experiments were performed in a 1-atm furnace and in a cold seal pressure vessel (CSPV). Experiments at 1 atm were conducted in gas mixtures containing H_2-Ar-CO_2-CO-H_2O. The diameter of the inner tube used was 4 cm. Oxygen fugacity was constantly monitored with a solid zirconia electrolyte probe flushed with air. Cylinders were suspended with platinum wire. Because of the high viscosity at experimental conditions, the sample did not deform significantly during the runs. Gas mixtures of H_2-CO_2 were used primarily, but specific runs were conducted with CO_2-CO and H_2-Ar combinations. Samples were loaded at temperature and the gas mixtures were introduced into the furnace within a few seconds. Depending on temperature, 3 to 10 min were required for the electromotive force (EMF) of the zirconia probe to reach a steady value. After the desired run duration, rapid drop quenches were performed without interrupting the gas flow.

Table 2. Description of the experimental conditions and results for the 1 atm experiments.

No.	Gas mixtures	fH_2[a]	log fO_2[b]	fO_2 ΔIW[b]	Duration (min)	Front position (μm)[c]
1 atm furnace, 800°C						
1	CO_2/CO	0	−19.15	−0.36	4320	0
2	CO_2/CO	0	−19.15	−0.36	10080	0
3	Ar/H_2	0.02	−19.15	−0.36	1920	85
4	Ar/H_2	0.02	−19.15	−0.36	3288	110
5	CO_2/H_2	0.25	−18.20	+0.6	2886	240
6	CO_2/H_2	0.25	−18.20	+0.6	6060	320
7	CO_2/H_2	0.5	−19.15	−0.36	180	125
8	CO_2/H_2	0.5	−19.15	−0.36	390	205
9	CO_2/H_2	0.5	−19.15	−0.36	2340	450
10	CO_2/H_2	0.5	−19.15	−0.36	4020	605
11	CO_2/H_2	0.5	−19.15	−0.36	7020	800
1 atm furnace, 700°C						
12	CO_2/H_2	0.7/0.5	−22.10	−0.70	180	105
13	CO_2/H_2	0.7/0.5	−22.10	−0.70	360	170
14	CO_2/H_2	0.7/0.5	−22.07	−0.67	1320	310
15	CO_2/H_2	0.7/0.5	−22.07	−0.67	4444	560
16	CO_2/H_2	0.7/0.5	−21.17	−0.77	7295	730
1 atm furnace, 600°C						
17	CO_2/H_2	0.67/0.5	−24.85	−0.25	360	140
18	CO_2/H_2	0.67/0.5	−24.85	−0.25	1350	240
19	CO_2/H_2	0.67/0.5	−24.60	0	4020	440
20	CO_2/H_2	0.67/0.5	−24.60	0	5778	530
1 atm furnace, 550°C						
21	CO_2/H_2	0.67/0.5	−26.4	+0.1	1200	170
22	CO_2/H_2	0.67/0.5	−26.4	+0.1	2610	265
1 atm furnace, 500°C						
23	CO_2/H_2	0.65/0.5	−28.5	+0.14	2400	185
24	CO_2/H_2	0.65/0.5	−28.5	+0.14	4800	280
1 atm furnace, 300°C						
25	H_2	1	?	?	4320	60

[a] The higher value is the fH_2 introduced into the furnace and the lower value is the fH_2 in the case where equilibrium between H_2-CO_2 mixtures is attained.

[b] At temperatures below 700°C, the fO_2 is probably uncertain and the fH_2 value are bracketed.

[c] The front position was optically defined as the first change in color noticeable within the glass. At low fH_2, the color change is progressive, whereas as fH_2 becomes higher than 0.5 bar, the color change becomes more and more abrupt. Error in the definition of this front was of ~10 μm at $fH_2 < 0.5$ bar and 5 μm at $fH_2 > 0.5$ bar.

The temperature range of the experiments was 300 to 800°C. Fast vesiculation of the obsidian due to gas (water) overpressure was observed near 870 to 890°C, which forced restriction of the temperature to below 800°C (given the long run durations). Within this low-temperature range, there is the possibility that one of two problems may arise: first, the zirconia probe may read an anomalous fO_2 value as a result of the high impedance of the probe at these conditions; and second, H_2-CO_2 mixtures are expected to undergo disequilibria because the reaction $H_2 + CO_2 \rightarrow H_2O + CO$ may not reach equilibrium (Beckett and Mendybaev, 1997). It follows that the experimental fH_2 may be higher than that expected for a given H_2/CO_2 ratio as temperature changes. This was tested by monitoring the fO_2 output of the zirconia probe for a constant gas composition ($H_2/CO_2 = 0.6 \sim$ IW + 0.2 at 1000°C) at different temperatures (1000 to 500°C). By using the tables of Deines et al. (1974), we calculated the theoretical T-fO_2 path and compared it with the fO_2 measured by the zirconia probe. From 1000 to 750°C, the deviation did not exceed 10 mV corresponding to less than 0.2 log unit of fO_2. Between 750 to 600°C, the fO_2 values measured were consistently lower than those expected, with a discrepancy of 0.6 to 1 log unit of fO_2, and below 600°C, the measured fO_2 values were in reasonable agreement or slightly overestimated. The high resistance of the zircon probe is almost certainly the main reason for this discrepancy, and therefore, we decided to rely on the gas ratio. However, gas disequilibria must also affect the measurements. As will be shown in the Results, fH_2 rather than fO_2 is the driving parameter that must be correctly determined. We decided to conduct our measurements at different temperatures with gas mixture compositions theoretically corresponding to the desired equilibrium fH_2. To limit the extent of gas disequilibria, we conducted experiments at a low total flow rate (170 mL · min^{-1}). We then considered that the fH_2 during the runs was between the percentage of H_2 initially introduced into the furnace and the equilibrium fH_2 (Table 2, runs 12 to 24).

In the CSPV, experiments were performed in the temperature range 700 to 1000°C, in TZM alloy bombs (molybdenum rich) with Ar used as standard pressure medium. The internal temperature had been calibrated against the temperature of the furnace. For all experiments, the temperature accuracy is estimated to be within ±15°C. Obsidian cylinders were placed in Au capsules that were open to the atmosphere within the vessel. The vessels were filled with the desired fH_2, and pressure was then completed to 200 bar with argon (Table 3, runs 26 to 38). With samples in the cold zone, the vessels were heated to the

Table 3. Description of the experimental conditions and results for the high-pressure experiments.

No.	P_{H2}/P_{Ar} (bar)[a]	T°C	P_{tot} (bar)[b]	Total Durations (min)[c]	Durations at T (min)[d]	Front position (μm)[e]
26	10/200	800	240	90	0	0
27	2/200	800	220	98	8	70
28	5/200	800	230	105	11	125
29	8/200	800	230	97	11	211
30	12/210	800	250	107	7	250
31	12/210	800	250	107	11	310
32	22/210	800	265	96	6	310
33	27/200	800	225	97	4	255
34	35/200	800	240	93	5.5	440
35	52/200	800	265	96	5	560
36	20/200	800	230	150	60	>2000
37	5/200	700	220	98	12	108
38	5/200	1000	250	96	7	140

[a] Pressure of H_2 and argon initially loaded in the vessel. For run 26, 10 bar of H_2 was first introduced, and then the pressure was completed with argon to 200 bar.
[b] Total pressure measured at dwell temperature.
[c] Duration of the exposure of the sample to pressure (including heating time).
[d] Duration of the exposure of the sample to both pressure and temperature.
[e] See Table 2.

dwell temperature within less than 90 min, and the sample was then directly placed into the hot spot of the vessel with a magnet and support rod. We estimated that the sample was heated within a few seconds. By using the magnet, experiments were quenched by moving the sample to the cold part of the vessel. The temperature of the sample dropped to 25°C within a few seconds. On the whole, run duration including the heating step was less than 2 h and 30 min, with a maximum of 60 min at dwell temperature. It was therefore assumed that H_2 loss in the wall of the vessel occurred to only a small degree (Schmidt et al., 1995). In addition, it must be stressed that most of the runs lasted less than 20 min (Table 3, runs 26 to 38).

After experiments, glass cylinders were cut into wafers and underwent double polishing for optical observation, Fourier-transform infrared (FTIR) spectroscopy, electron microprobe analyses (EMPA), and Mössbauer spectroscopy. Changes in the color of the glass were identified as changes in the iron redox ratio, as observed by Gaillard et al. (2002, 2003). Therefore, the inward progression of a change of color within the run products was optically monitored and used to monitor the reaction rate. FTIR spectroscopy was conducted to identify volatile content and diffusion profiles in the glasses. Spectra were measured with a Bruker IFS 120 HR high-resolution FTIR spectrometer coupled with a Bruker infrared microscope containing all-reflecting Cassegrainian optics and with a tungsten light source, CaF_2 beam splitter, and a high-sensitivity, narrow-band MCT/A detector. A beam diameter at the focus plane of 60 μm was used, and 200 scans were performed over the frequency range 7500 to 2000 cm^{-1}. Water-derived species were measured from the heights of the 3500- and 4500-cm^{-1} bands by means of the extinction coefficients of Newman et al. (1986). The 4500- and 5200-cm^{-1} bands were used to qualitatively specify the nature (OH or H_2O) of these species. Molecular H_2 bands were observed in some cases in the run products at 4150 cm^{-1} and were used qualitatively (Schmidt et al., 1998). EMPA was used to identify the possible chemical migration of major elements associated with the ongoing reactions. The operating conditions were 15 KeV, 6 nA, 10 s of counting on the elements peaks, and 5 s on the background with a defocused beam (25 μm). Analyses that used the Mössbauer milliprobe (McCammon et al., 1991; McCammon 1994) were performed on selected samples with a spot size of ~300 μm to determine Fe^{3+}/Fe^{tot} in the two regions of sample with different colors.

4. RESULTS

Tables 2 and 3 summarize the conditions and results of experiments conducted in a 1-atm furnace and a CSPV, respectively. Gas mixtures, fH_2, fO_2, T, durations, and the advancement of the reaction are specified. From examination of run products with a polarizing microscope, it appears that whatever the run duration, no increase in the crystal content was observed. EMPA revealed that no major changes of chemical composition were observed apart from a slight decrease of ~3 to 8% relative to Na content as a result of volatilization of Na_2 in the gas phase. The migration of Na was previously reported by Gaillard et al. (2003) for experiments of this nature (for Na volatilization under dry conditions, see Georges et al., 2000). Except for the runs 1, 2, and 26, which showed no reaction, the reduction of iron was systematically visible through an abrupt color change between the reduced (translucent) and the pristine zone (dark) (Fig. 1). By use of micro-Mössbauer spectrometry, we were able to demonstrate that the reduced zone contained no detectable ferric iron, whereas the dark region showed the same ferric iron content as the starting product. The migration rates of boundaries between the two redox regions, called hereafter the redox front, were therefore used as an indicator of the reaction rate.

Experiments performed with different gas mixtures but at constant fO_2 are presented in Table 2 (nos. 1–4, 7–11). The fO_2 in question is 0.36 log units below the fO_2 imposed by the redox buffer iron–wüstite (IW). Such a reducing environment is not in equilibrium with the studied obsidian. However, in

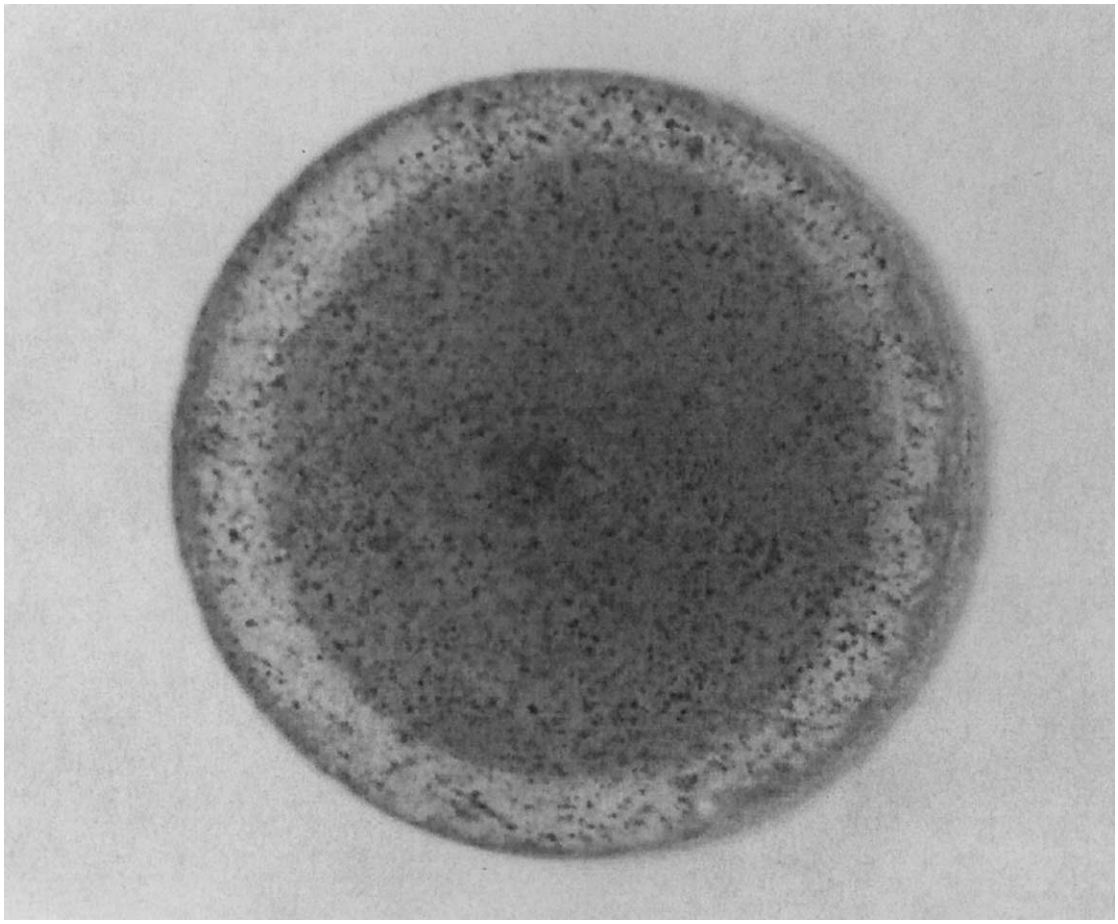

Fig. 1. Color changes due to reduction of ferric iron on the sample rims. The translucent external layer of ~500 μm corresponds to the reduced zone. The inner brown zone is pristine. Diameter of the sample is 4 mm. Sample 34. The black points are crystals entrapped in the glass matrix.

CO_2-CO mixtures, no changes of iron redox state and no chemical migration were observed within the samples, even after 1 week of run duration. In Ar-H_2 mixtures containing 2% of H_2 (fH_2 = 0.02 bar, nos. 3, 4), a narrow zone of reduced glass, ~100 μm, was observed at the sample rim after 2 days. In contrast, for H_2-CO_2 mixtures adjusted for the same fO_2, the fH_2 equals 0.5 bar and the reduction front had already advanced over more than 100 μm in less than 3 h. Experiments performed in H_2/CO_2 but at lower fH_2 (0.25 bar) showed a slower reaction rate (compare no. 5-6 with no. 7-11 in Table 2). Results from experiments in the CSPV (Table 3) showed that increasing fH_2 strongly increases the reaction rate, as seen for run 35. For this experiment, 52 bar of H_2 was loaded into the vessel, and the reaction progressed over a distance of 560 μm within 5 min. These results indicate that the partial pressure of H_2 in the gas is apparently one of the chief parameters driving the reaction rate.

Along the reduced region, FTIR profiles (Fig. 2) revealed an increase in OH content, and for experiments performed at high fH_2, molecular H_2 was also detected (Schmidt et al., 1998). For experiments performed in the 1-atm furnaces, no H_2 was detected, and the increase in OH content was lower. Figure 3 shows an OH profile across the entire sample synthesized at 1 atm. The hydroxyl content is very low at the sample rim, reaching a maximum near the redox front, whereas the inner zone displays the same water content as the starting product. For experiments performed under pressure, the chemical profiles are obviously different (Fig. 4): The OH content reaches a maximum at the sample rim, lying between 0.17 to 0.19 wt%, independent of the applied fH_2, and decreases as it approaches the reduction front, which was observed optically, the shape of the hydroxyl profile being downwardly concave in nature. For runs with $fH_2 > 10$ bar, an infrared peak was observed at 4150 cm^{-1} as a result of molecular H_2 vibrations. An H_2-profile is shown in Figure 4. The penetration of H_2 into the sample was always less than that of the reduction front and the OH front.

5. INTERPRETATION

5.1. Rate Law

The linear relationships obtained from Figure 5, where the square of the reduction front progression is plotted against run duration, indicate that the reduction of ferric iron is diffusion limited in the temperature range 500 to 800°C. The slopes of the curves in Figure 5 give the rate constant (K) of the overall process of reduction calculated as

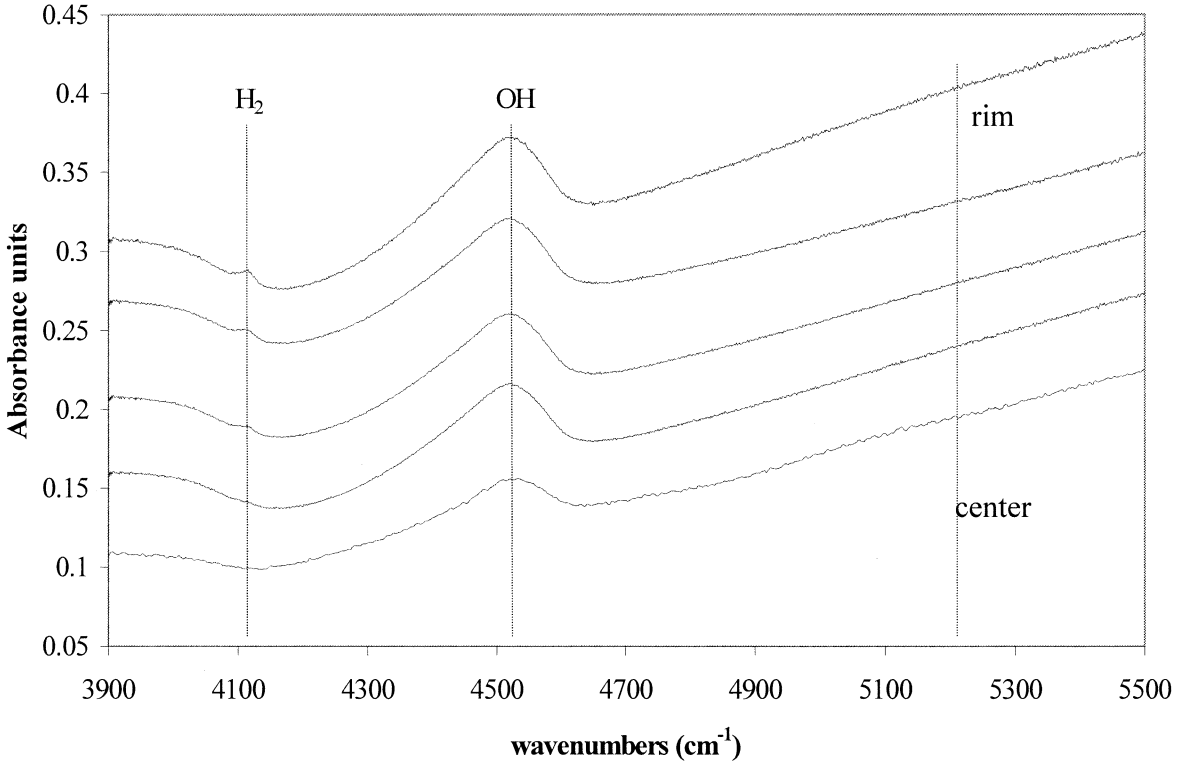

Fig. 2. Infrared spectra of sample 34. Upper spectra correspond to the sample rims and lower spectra were collected in the sample inner part. Note the absence of molecular H_2O bands at 5200 cm^{-1} and the progressive vanishing of the H_2 bands going from rim to center.

$$\xi = R_0 - (Kt)^{1/2} \quad (3)$$

where ξ is the front position as measured from the sample rim, R_0 is the cylinder radius, and t is time. Additional details concerning the meaning of the constant K are given below in the text. It is clear that adsorption–diffusion at the surface or even reaction within the melt are not rate limiting. Because diffusion processes have, in general, lower activation energies than reaction processes (Cussler, 1997), we expect that diffusion will rate-limit even at higher temperatures.

The effect of fH_2 on the reduction rate of ferric iron is shown in Figure 6. The experimental data of Gaillard et al. (2003) is also shown and will be further discussed below. The rate constant increases abruptly from 0 to 10 bars fH_2, whereas above 10 bars, it increases slowly. The shape of the curve indicates that the reduction rate is in fact limited by the rate of H_2 supply. This supply is related to both H_2 diffusion and solubility in the melt, with the latter being a function of fH_2.

Mössbauer and FTIR data revealed that the amount of ferric iron that has been reduced is equal to the difference in OH content in the reduced, compared with the pristine volume (more precisely, the amount of OH at the sample rim minus the OH content in the center: On Fig. 4, 0.18 to 0.13 wt%. This quantity, although slightly higher, corresponds to the amount of Fe^{3+} that has to be reduced).

5.2. Modeling

The redox reactions that take place can be then written as follows:

$$H_2 \Rightarrow 2\,H^+ + 2\,e^- \quad (4a)$$

$$2\,Fe^{3+} + 2e^- \Rightarrow 2\,Fe^{2+} \quad (4b)$$

Crank (1975, p. 305) gives a mathematical solution describing the velocity of a reaction front when a mobile species diffuses and reacts instantaneously with a medium yielding a nonmobile species. The time-dependent front position (ξ) is therefore a function of both solubility and diffusivity of the mobile species:

$$\xi = 2\alpha(DH_2t)^{1/2} \quad (5)$$

with α, in our case, defined as

$$S_{H_2}/(1/2\ C_{OH}\ \rho) = \Pi^{1/2}\ \alpha \exp(\alpha^2)\ \mathrm{erf}(\alpha) \quad (6)$$

S_{H_2} defines the H_2 solubility and C_{OH}, the part of the H_2 molecule that has reacted to form immobilized OH groups, the latter being equal to the concentration of ferric iron that has been reduced to ferrous iron. ρ is the density of the melt required if solubility is expressed as mass per unit volume. The front velocity ξ can be calculated by solving α from Eqn. 6 and introducing it into Eqn. 5. Basically, a given S_{H_2}/C_{OH} ratio corresponds to a unique value of α. However, we cannot directly calculate α because no solubility law is available for calculating S_{H_2} in a rhyolitic system under these experimental conditions. However, data in Tables 2 and 3 provide constraints on ξ, t, and fH_2. From FTIR data, COH is known, so we can extract, through simultaneous mathematical manipulation of Eqns. 5 and 6 for each run, values for α, diffusion, and solubility of H_2. A minimization routine was operated on Eqns.

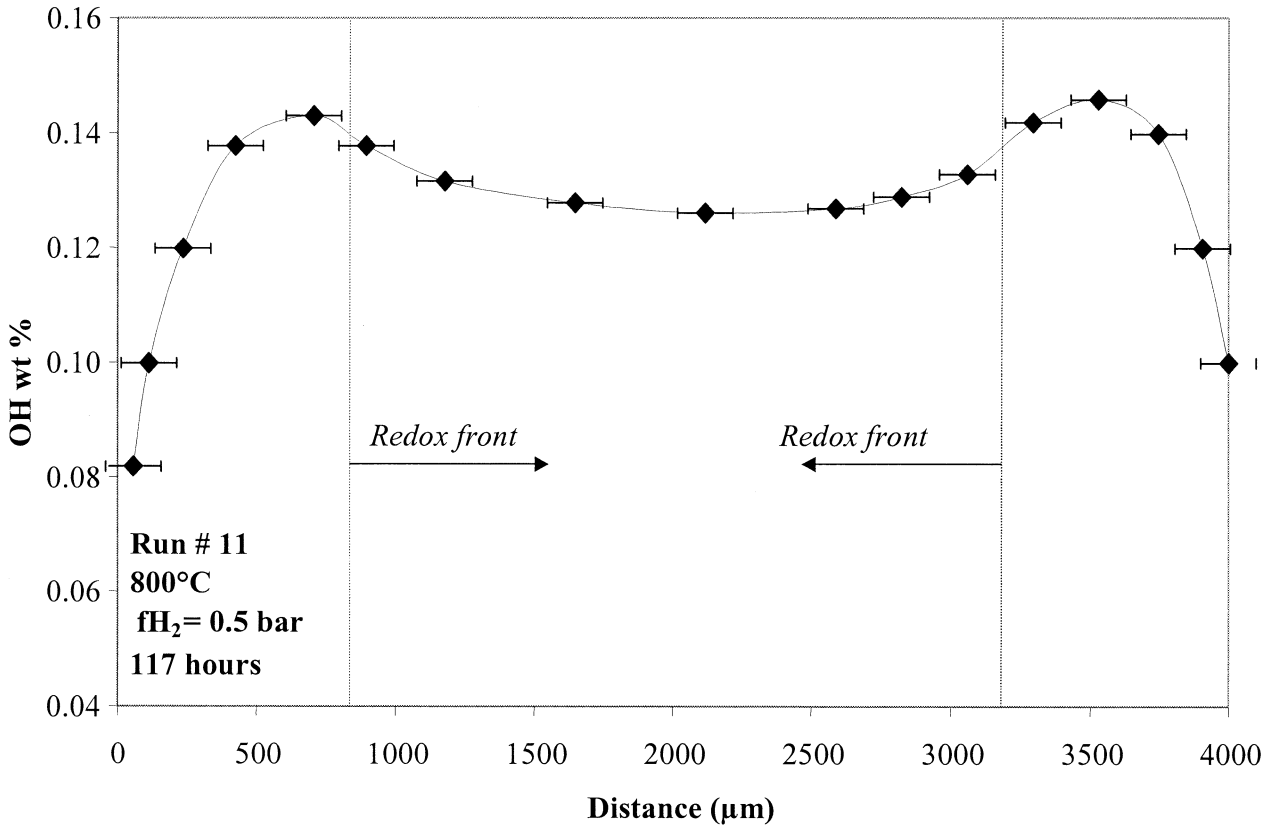

Fig. 3. Typical "low H_2 pressure" hydroxyl profiles obtained from infrared spectra of run product 11. Note the decrease of OH on the sample rims and the position of the OH front in front of the redox front. See text for discussion.

5 and 6 to reproduce the experimental observation (ξ, for a given t, T, fH_2), taking both solubility and diffusion of molecular H_2 as unknowns. To estimate S_{H_2} for each run, we impose a solubility law of the form $S_{H_2} = a fH_2^{\,b}$, where a and b are constants estimated from the model. The diffusion rate of molecular H_2 in the glass/melt is considered to be constant for a given temperature. In our procedure, the fH_2 of experiments shown in Table 3 was allowed to vary within the calculated uncertainty. Calculations were performed considering that fH_2 is higher than the amount of H_2 initially introduced into the vessel (Table 3), this being due to a temperature and pressure increase. The final fH_2 should be equal to $fH_2 = fH_2^{\text{initial}} P_{tot}^{\text{final}}/P_{tot}^{\text{initial}}$, ±20%. This accounts for the fact that an fH_2 increase should occur proportionally to the increase in pressure that was measured during heating (Table 3, column P_{tot}). The uncertainty, ±20%, could account for possible heterogeneities in the molecular H_2/Ar ratio within the vessel. Thermal and/or gravitational segregations may affect the fH_2, and we estimated that a maximum 20% fluctuation of fH_2 around the mean value, as described above, was possible. Molecular H_2 diffusion through the wall of the vessel may decrease the fH_2 value during the runs, but as a result of the short run duration, we consider that this exchange should not exceed 5% of the H_2 initially introduced into the vessel (see Schmidt et al., 1995). The fugacity coefficient for H_2 was set equal to 1, given the low pressure of the experiments. In Table 4 and Figure 6, we present results of the calculation including fH_2, S_{H_2}, calculated and measured K values (see footnote of Table 4), and the corresponding value for α. The best fit was obtained when a solubility law for H_2 of the form $S_{H_2} = a fH_2^{\,b}$ was used with b = 1.2 (compare sixth column with the last one in Table 4). The data of Gaillard et al. (2003) obtained on a strongly peralkaline silicate melt, Eburru (Eb), was also included in Table 4 and Figure 6. Despite the difference in melt composition and Fe^{3+} content between our metaluminous rhyolite and the peralkaline melt of Gaillard et al. (2003), the kinetic model

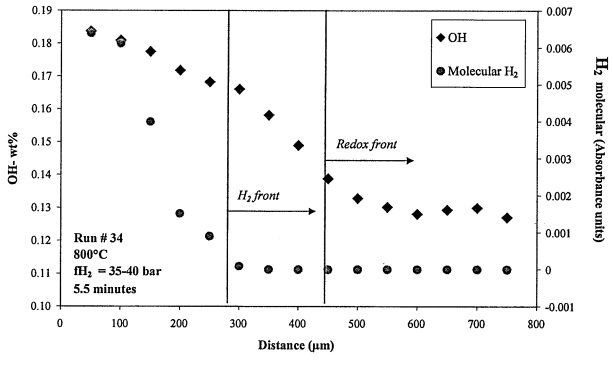

Fig. 4. Typical "high H_2 pressure" profiles of H_2 and OH in the glass obtained from infrared spectra of sample 33. Note the difference between the positions of the H_2, OH, and redox fronts. See text for discussion.

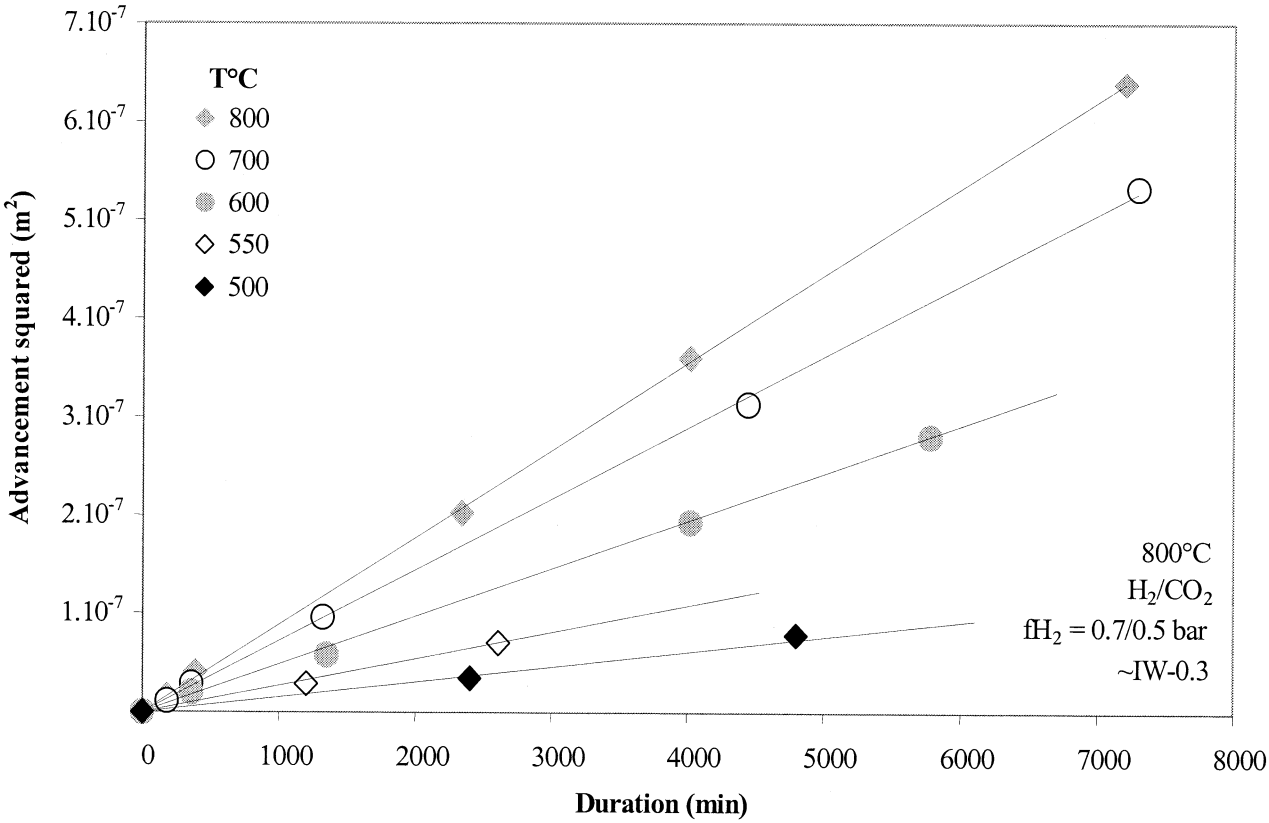

Fig. 5. Characterization of the rate laws governing the reduction rate of ferric iron from 800 to 500°C. The square of the reduction advancement is linearly dependent on run durations: there is evidence for a diffusion-limited process. The reaction advancement, ξ, is calculated as $\xi = R_0 - (k \cdot t)^{1/2}$ (see Eqn. 3).

is able to predict the experimental points, with similar solubility and diffusivity laws for H_2 in the melt/glass. It must be stressed that the viscosity of the Eburru melt is similar to the viscosity of basalt under the same conditions (P, T, H_2O content, NBO/T = 0.4). This implies that both solubility and diffusivity of H_2 in silicate melts are not significantly affected by the composition or the structure of the melt.

5.3. Temperature Effect

From the slope of the curves in Figure 5 and the results of runs 28, 37, and 38, the temperature dependence of the reaction rate, which hereafter is called the activation energy because this is a diffusion-limited process, can be extracted. Figure 7 shows the rate constant plotted as a function of inverse temperature for $fH_2 = 0.5$ and 5 bar. The activation energy extracted from the two sets of data, 40 ± 6 kJ/mol, is very small when compared with diffusion of other volatiles in melts. Lee and Fry (1966) and Lou et al. (2003) estimated activation energies for H_2 diffusion in fused silica as ~43 kJ/mol, this being in good agreement with our findings. Helium diffusion in rhyolites has a comparable activation energy, ~38 kJ/mol (see review of Watson, 1994). Our value for this activation energy is consistent with the general trend for diffusion of neutral species (H_2O, CO_2, Ar, Ne, He) whose activation energies positively correlate with the radius of the diffusing species (Watson, 1994). These points therefore give credence to the starting hypothesis that neutral molecular H_2 diffusion in the melt indeed controls the reaction rate. However, our findings are very different from those of Chekmir et al. (1986) who calculated an activation energy of 113 kJ/mol for H_2 diffusion in molten albite, this being slightly higher than 103 kJ/mol, the value obtained for H_2O diffusion in natural rhyolites by Zhang et al. (1991). We think it unlikely that H_2 and H_2O diffusion could have similar activation energies given their difference in molecular size and we therefore consider the high activation energy found by Chekhmir et al. (1985) to be flawed. It should be noted that the temperature dependence of H_2 solubility was not taken into account in either this study or the study carried out Chekmir et al. The low activation energy calculated might be the consequence of a negative temperature dependence of S_{H_2}, as suggested by the findings of Schmidt et al. (1998) in SiO_2 glass. From our data, it is not possible to discriminate between the effect of temperature on H_2 solubility and the effect on diffusion. We maintain that we have predicted correctly the temperature dependence of the rate of H_2 supply at the reaction front.

It is worth noting that the activation energy calculated is constant over a temperature range spanning the glass transition temperature (~850°C). The data points for both the melt and glass regions can be modeled by the same parameters (Fig. 7). The reduction rate of the Eburru sample (Table 4, Fig. 6; see

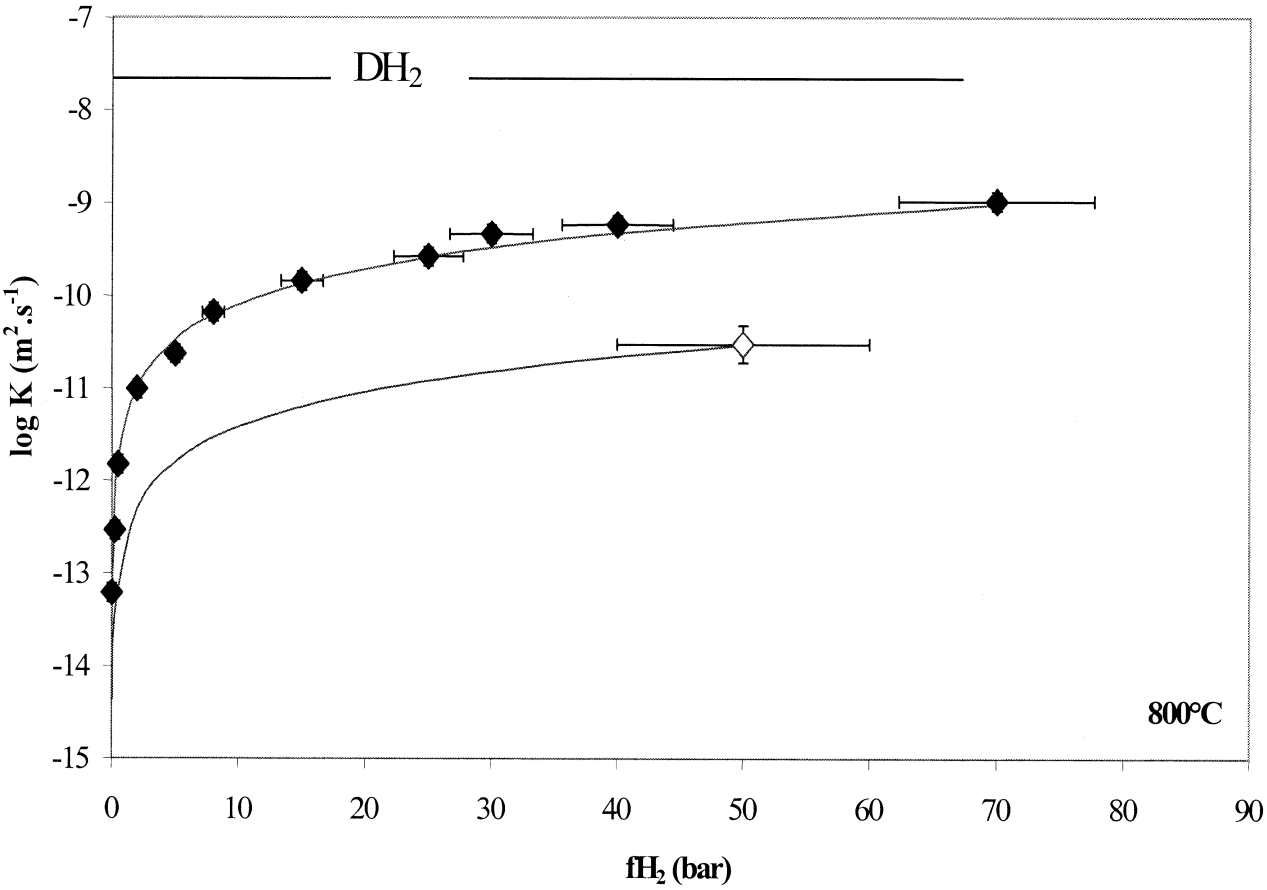

Fig. 6. Characterization of the fH_2 dependence of the reduction rate of ferric iron at 800°C. The shape of the curves indicates that the reduction rate is controlled by the solubility of H_2 in the glass (at 800°C, the obsidian is still in the glassy state). Black diamonds = points obtained in this study; open diamonds = data of Gaillard et al. (2003) on the Eburru sample (Table 3, sample Eb). The solid line is the calculated H_2 diffusion at 800°C. The solid lines fitting the data points correspond to Eqns. 5 and 6.

Table 4. Extraction of the reaction constants at T = 800°C and parameters of the model including, diffusivity and solubility law for molecular H_2.

No.	fH_2	SH_2 (gr.m^{-3})	SH_2 (ppm-wt)	log K measured[a]	log K calculated[b]	α	log K calculated[c]
3–4	0.02	0.002	0.001	−13.21	−13.56	0.0005	−12.89
5–6	0.25	0.058	0.025	−12.54	−12.15	0.0026	−11.80
7–11	0.50	0.14	0.06	−11.83	−11.76	0.0040	−11.49
27	2	0.8	0.4	−11.01	−10.98	0.0099	−10.89
28	5	2.6	1.1	−10.63	−10.47	0.0179	−10.49
29	8	4.8	2.1	−10.18	−10.21	0.0242	−10.29
30–31	15	10.8	4.7	−9.84	−9.85	0.0364	−10.02
32	25	20.7	9.9	−9.57	−9.57	0.0505	−9.80
33	30	26.1	11.3	−9.33	−9.47	0.0568	−9.72
34	40	37.6	16.3	−9.23	−9.30	0.0684	−9.59
35	70	76.9	33.4	−8.98	−8.99	0.0980	−9.35
Eb	50	50.0	21.7	−10.52	−10.53	0.0215	−11.17

$SH_2 = 0.34\ fH_2^{1.28}$ (g/m^3)

log $DH_2 = -7.8$ m$^2 \cdot$ s^{-1} at 800°C, and $DH_2 = 1.40\ 10^{-6} \exp[-40000/(RT)] - (m^2 \cdot s^{-1})$

[a] K is the reaction constant deduced from experiments as $K = \xi^2/t$ (see Eqns. 3 and 5).
[b] Reaction constant calculated with $K = 4\ \alpha^2\ DH_2$ (see Eqns. 5 and 6) and a solubility law for molecular H_2 as $SH_2 = 0.34\ fH_2^{1.28}$.
[c] Reaction constant calculated with linear fH_2 dependence for solubility: $SH_2 = 6.58\ 10^{-4}\ fH_2$.

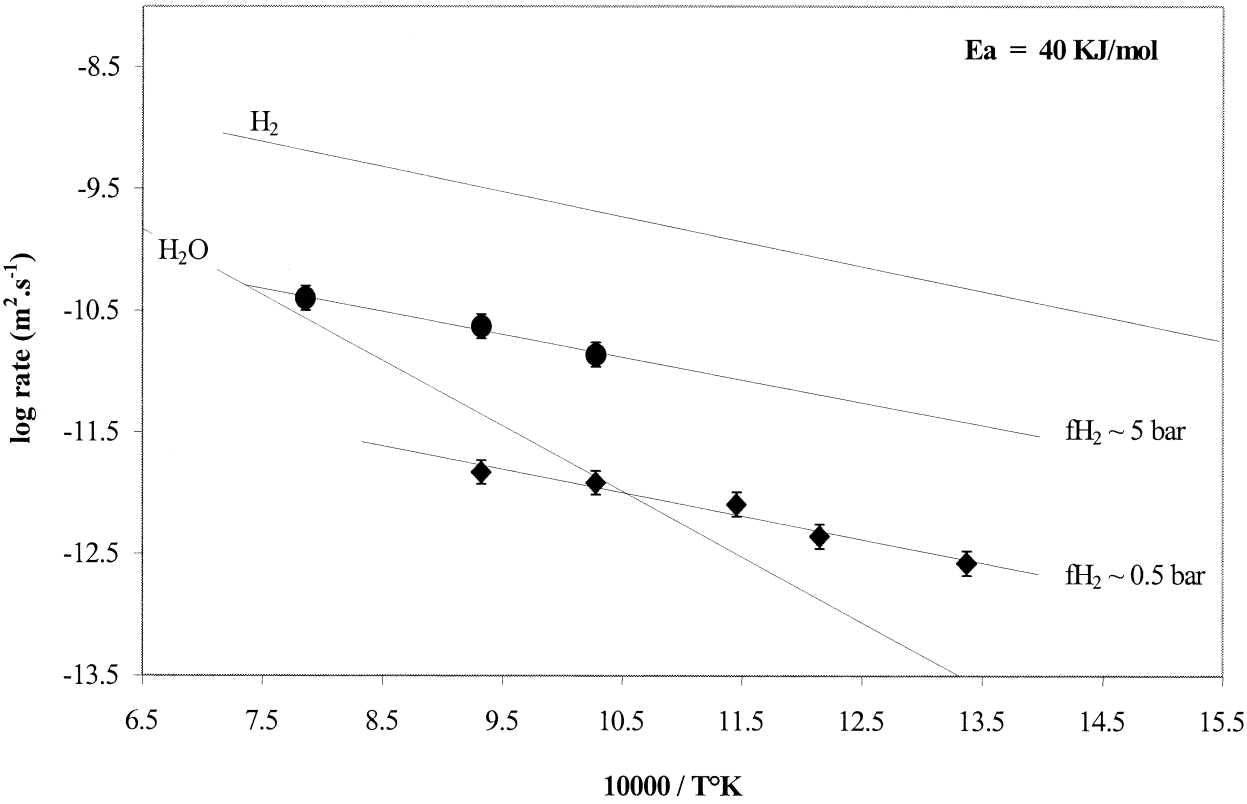

Fig. 7. Temperature dependence of the reduction rate determined at two different fH_2. The two fits to the data points are performed with the same activation energy (40 kJ/mol). Other lines correspond to the diffusion rate of molecular H_2O (Zhang et al., 1991) and molecular H_2.

also Gaillard et al., 2003), which is a melt at 800°C, is perfectly predicted by the set of parameters also applied to the glass. Such diffusion properties, being similar in both glass and melt regions, have already been mentioned for diffusion of neutral species in amorphous silicates (see Watson, 1994). We therefore suggest that our model can be used for magmatic processes affecting melt redox state as well as weathering processes affecting glasses containing industrial and nuclear wastes where the redox couple H_2/H_2O dominates the fluid component.

5.4. H_2 Solubility in Melts

The solubility law obtained has the form $S_{H_2} = a\,fH_2{}^b$, where a is Henry's constant and b is an empirical parameter accounting for the nonlinearity of the relationship. Persikov et al. (1990) gave a solubility law for H_2 in iron-free molten albite glass. The form of their solubility law is similar to ours but the b exponent they gave is equal to ~0.5, whereas ours is equal to 1.28 (Table 4, Fig. 8). The reason for this difference is probably because of the fH_2 range, 100 to 8650 bar, where their relationship was calibrated, in contrast with our range, 0.02 to 70 bar. The Persikov et al. (1990) solubility law was obtained by fitting the total H content in quenched glasses against the fH_2. It is well known that hydrogen can be incorporated into a melt in the form of both proton and molecular H_2. It is therefore probable that their law calculates both H^+ and H_2 concentration in melts for a given fH_2. This might explain why Persikov et al. overestimate the solubility of H_2 at low fH_2 (Fig. 8). Nevertheless, there is reasonable agreement when both models are used at fH_2>70 bar. For example, H_2 solubility calculated from both models at fH_2 = 70 bar yields values differing by a factor of ~2, 68 ppm for Persikov et al. vs. 33 ppm for this study, and at fH_2 = 100 bar, 81 ppm for Persikov et al. vs. 53 ppm for this study. However, because fH_2 in natural magmas is more in the range 0.02 to 70 bar than 100 to 8650 bar, the use of our solubility law to simulate natural processes taking place in magmas is more relevant.

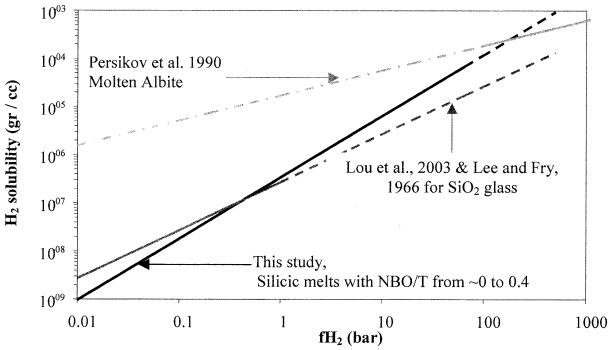

Fig. 8. Solubility laws for H_2 in silicate glasses and melts at 800°C. Different solubility relationships corresponding to different studies and different glass compositions are plotted. Sold lines = calibration domain of each study; dashed lines = extrapolations.

Molecular H_2 solubility was investigated in fused silica by Lee and Fry (1966) and recently by Lou et al. (2003). Their solubility data were fitted to show a linear fH_2 dependence and a slightly negative temperature dependence (the latter being almost negligible). Between 0 and 1 bar fH_2, which is within the range of investigation of their study, the calculated H_2 solubilities that used both models show remarkable agreement (Fig. 8). When extrapolated to higher fH_2, the predicted H_2 solubilities begin to diverge but remain in reasonable accord.

The solubility law determined in this study applies to both fully polymerized (SiO_2), as well as to high NBO/T liquids (Eburru composition; see Gaillard et al., 2003). These findings show good agreement with the observation that the solubility of neutral species becomes less dependent on the ionic porosity (~NBO/T) as the size of the neutral molecule or atom decreases. For example, Helium solubility varies by a factor of less than two between rhyolite and komatiite, whereas Argon solubility varies by a factor of 100 under conditions that are otherwise the same (Carroll and Webster, 1994). In the case of H_2 we have shown that solubilities in SiO_2 glass, metaluminous obsidian, molten albite and strongly peralkaline obsidian compare fairly well. We therefore expect that our solubility law for H_2 applies to most composition ranges covered by natural magmas.

5.5. Diffusion Profiles

In this section, diffusion profiles are only qualitatively discussed. The OH profiles shown in Figure 3 and 4 differ because the latter hydroxyl groups produced by the reaction are measured only in the reduced part of the sample, whereas for the former, reaction-derived OH bands are also observed in advance of the reduction front. Because of the slow reaction rate at $fH_2 = 0.5$ bar, the sample, whose profile is shown in Figure 3, was exposed to high temperature for a long time at room pressure. Under these conditions, the velocity of the reduction front and the rate of OH production were slower than the diffusion of molecular H_2O, as can be seen on the Arrhenius diagram (Fig. 7). It follows that the reaction-derived OH migrates in the form of H_2O (Zhang et al., 1991) in response to the chemical potential gradient. Diffusion toward the rim before degassing occurs but diffusion in front of the redox front also occurs as a result of C_{OH} in this front being higher than in the sample core. At higher fH_2 the reaction rate is much faster than the migration rate of H_2O molecules so the reaction-derived OH can be considered as immobile (Fig. 4). As the reaction products at these conditions are not immobile with respect to the velocity of the redox front, the kinetic model used (Eqns. 5 and 6) should not apply anymore. It is apparent from Table 3 that the reaction constants are not as well calculated for low fH_2 as for high fH_2 conditions (see Table 3, compare $fH_2<1$ and >1). However, the extreme sensitivity of the reaction rate to the fH_2 in the low fH_2 region is difficult to reproduce exactly and we therefore consider the agreement between calculated and measured values acceptable. For this reason, we assume that the migration of reaction products during the ongoing reaction does not significantly affect the overall reaction rate and its kinetic law.

The apparent lag of the H_2 front with respect to the OH and redox fronts, as shown in Figure 4, may suggest that H_2 diffusion is slower so meaning that the velocity of the redox front is controlled by the OH front. However, the extremely reducing conditions imposed by the presence of several bar of H_2 in a melt having a very low water activity, created a strong displacement toward the right hand side of the following equilibria:

$$H_2 + 2\,Fe^{3+} \Leftrightarrow 2\,Fe^{2+} + 2\,H^+ \text{ or}$$

$$H_2 + 2\,FeO_{1.5} \Leftrightarrow 2\,FeO + H_2O \quad (7)$$

It follows that H_2 and Fe^{3+} are very reactive and cannot coexist (which may not be the case when significant amounts of water are dissolved in the melt). Therefore, the extent of H_2 penetration, observed in Figure 4, in fact reflects the stability of H_2, where nearly all ferric iron has been reduced to satisfy the equilibrium 7. Subsequently, the hydroxyl front is evidence of the reacted H_2 course, and therefore, the OH profile is a mirror image of the ferric iron profile. According to Crank (1975 see chapter concerning diffusion and chemical reactions), the unusual shape of the OH profile (downward and concave in nature, classically interpreted as a composition dependent diffusion coefficient) is interpreted here as a diffusion + reaction (immobilization) process: The OH representing the immobilized molecules. The ambiguity comes from the fact that whatever the fH_2 was, the redox front marked on the Figure 4 by a vertical line is positioned systematically in front of the OH profile. This means that ferric iron should still exist behind the redox front and the latter is in fact evidence of the beginning, rather than the completion, of Fe^{3+} reduction.

5.6. Diffusion vs. Reaction Limited

In a previous article, Gaillard et al. (2002) concluded that oxidation–reduction of iron was a reaction limited process because they observed a delay between DH_2 and the rate of iron redox changes and because they observed no color changes across the run products. From Gaillard et al. (2003) and this study, it appears that the redox reaction operating at the redox front does not limit the overall reduction rate independent of the fH_2 and T. However, the two half-redox reactions written in (Eqn. 4) indicate that one H_2 must react with two Fe^{3+} ions. It follows that this reaction should be limited by the ability of two Fe^{3+} ions to assemble before reacting with a H_2 molecule. However, this scenario may be ruled out as under our experimental conditions (mainly <800°C), Fe^{3+} diffusion must be $\ll 10^{-18} m^2 \cdot s^{-1}$, and therefore, this process should require a significant amount of time, given the distance between two ferric iron atoms in the melt/glass (>35 Å, compiling molten oxide partial volumes from Lange and Carmichael, 1990; Holtz et al., 1995 and Knoche et al., 1995, and assuming a random distribution of ferric iron). It is therefore likely that an intermediate species between H_2 and H^+ operates the electronic transfer between two ferric iron atoms. This intermediate step could be written as;

$$H_2 + Fe^{3+} \rightarrow Fe^{2+} + H_2{}^+ \text{ followed by } H_2{}^+ \rightarrow 2\,H^+ + 1\,e^- \quad (8)$$

and a coupled jump of 1 H^+ and 1 e^- toward the next ferric iron neighbor. Iron, in this scenario, is an immobile species, but does not affect reaction rate. Therefore, proton motion should

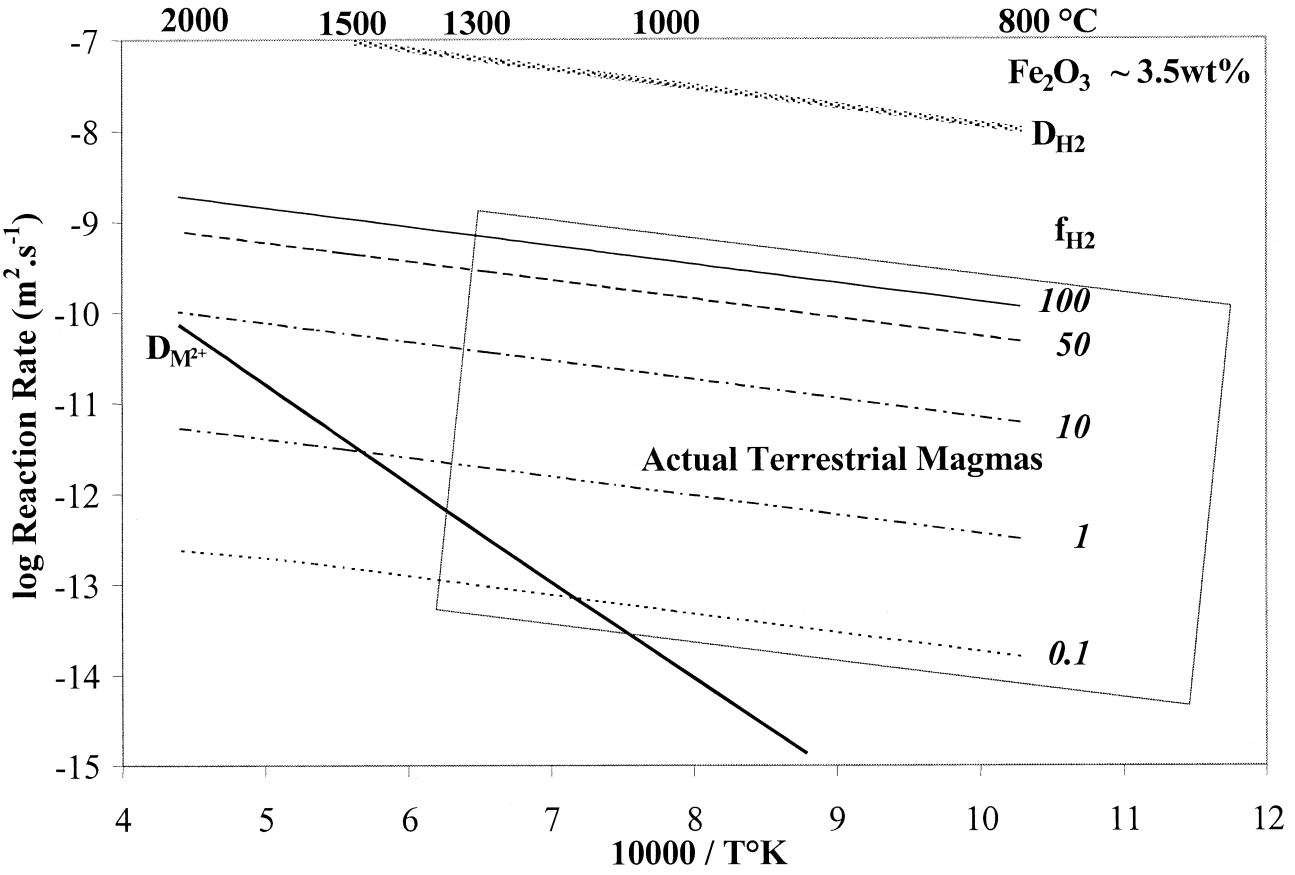

Fig. 9. Map of redox exchanges in glasses and melts as a function of temperature and fH_2. Rates of reduction or creation (by oxidation) of 3.5 wt% of ferric iron due to redox exchanges with H_2 are shown for hydrogen fugacity ranging from 0.1 to 100 bar. The line labeled DM^{2+} corresponds to the rate of a similar change of iron redox state controlled by diffusion of divalent cations as it operates in anhydrous systems (after Cooper et al., 1996, and considering a basaltic composition). The square corresponds to the fH_2-T domain of actual terrestrial magmas. It appears that in most of the fH_2-T conditions, the mechanisms of redox exchanges between iron and H_2 hydrogen is faster than the rate of redox exchanges rate limited by divalent cations migration.

occur, although Behrens and Nowak (1997) showed it to be a nonmobile species relative to H_2O mobility. A short jump is probably the best description of this phenomenon.

5.7. Oxidation Rate

According to Gaillard et al. (2002), the rates of oxidation and reduction of iron in water-bearing melts are similar. We therefore interpret the rate and mechanisms of oxidation as a mirror image of the reduction process we identify in this study: It will be controlled by the rate of H_2 extraction from the melt, this being a function of DH_2 and S_{H_2}. In the case of reduction, S_{H_2} is a function of the externally imposed fH_2. In the case of oxidation, the melt fH_2 is internally buffered by the equilibrium 7, and therefore, the outward H_2 flux will be controlled by this internally buffered fH_2. The equilibrium 7 shows that the buffered fH_2 is proportional to fH_2O and the ratio of the activities of $FeO/FeO_{1.5}$. In Figure 6, the horizontal axis (fH_2) can be replaced by $fH_2O/K_{(7)} \cdot a_{FeO}/a_{FeO1.5}$ to give the rate of oxidation, $K_{(7)}$ being the equilibrium constant 7. An exception to this is thought to occur when the water content of the melt is very low. Reaction 8, when reversed to consider oxidation, imply that 2 protons have to assemble to react and give rise to H_2^+ or H_2. At very low OH content, the distance between two H^+ may be large enough for this step to rate limit the overall oxidation rate. In that case, the oxidation process will be reaction limited, and therefore, growth of an oxidized layer should be linear with exposure time.

6. REDOX EXCHANGES IN NATURE

In dry systems, oxidation and reduction of iron in melts and glasses are rate limited by divalent cation mobilities. In hydrogen-bearing systems, redox exchanges between H_2 and iron dominate the mechanisms because these have the fastest reaction path. However, we saw that the latter mechanisms display reaction rates that are strongly dependent on fH_2 and whose temperature dependence is minimal. Therefore, it is likely that for low fH_2 and high-temperature conditions, the oxidation–reduction processes that are rate limited by divalent cation migration, may be faster than redox exchanges with H_2, thus implying a change in the mechanism of redox potential equilibration with variation of temperature or fH_2. In Figure 9, we

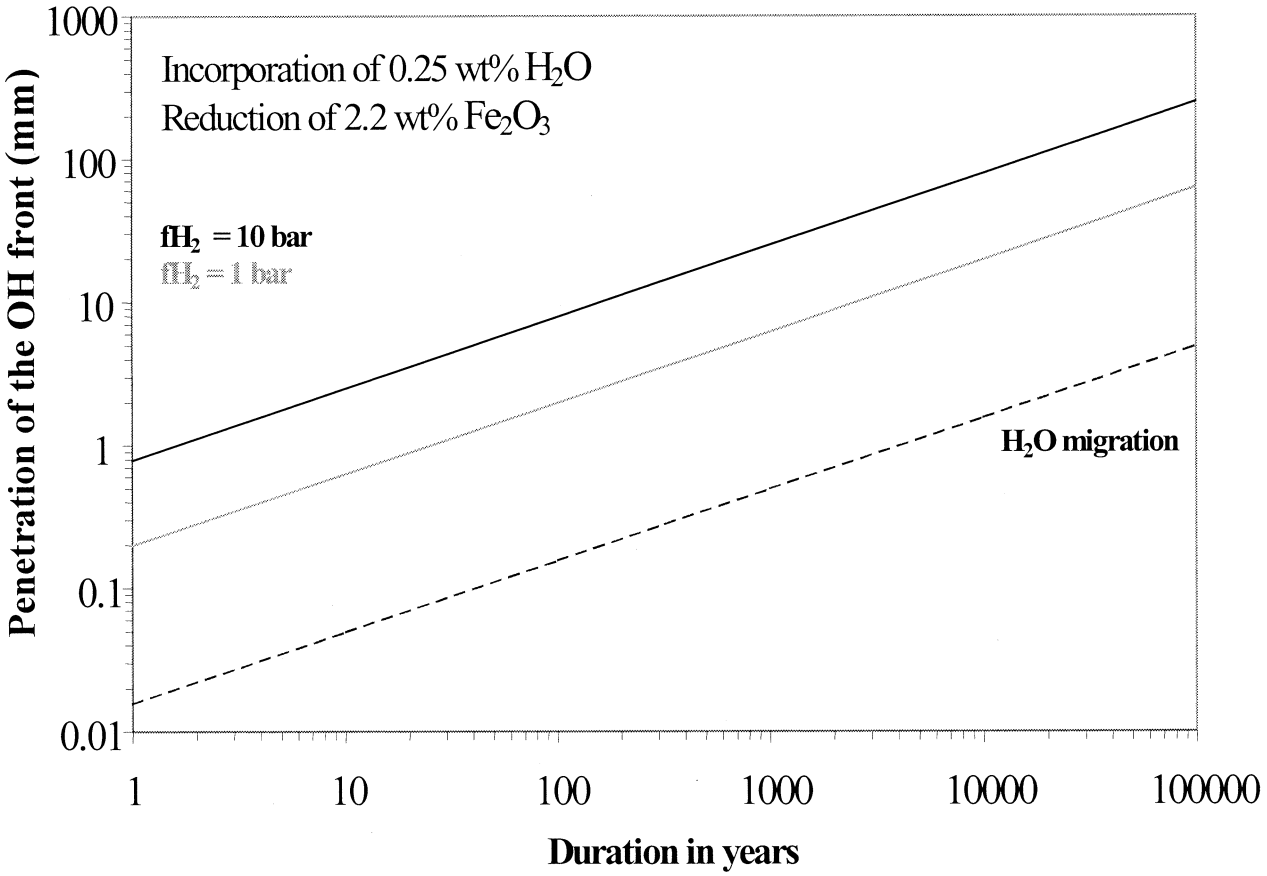

Fig. 10. The full lines illustrate the penetration of a front of 0.25 wt% of reduction-derived H_2O in a glass undergoing an exposure to different fH_2 conditions at 200°C under water-saturated conditions. The glass initially contains 2.2 wt% Fe_2O_3. For comparison, a front of hydration rate controlled by H_2O mobility is also shown (calculated after Zhang et al., 1991).

show a map of the rate of reduction or creation (oxidation) of 3.5 wt% ferric iron in a melt, as a function of temperature. We consider that this rate may be governed by either divalent cation migration (full line labeled DM^{2+} calculated after Cooper et al., 1996) or flux of H_2 through the melt operating at different fH_2. To read this map, one should consider that at a given temperature and fH_2, the faster mechanisms dominate. For example, at fH_2 equal to 0.1 bar and at low temperature, H_2 flow through the melt is rate limiting, whereas at temperatures around 1150°C and higher, redox exchanges are rate limited by divalent cation migration. Therefore, even in the presence of hydrogen, the redox mechanisms applying in dry systems are likely to operate. Figure 9 also shows the fH_2-T domain of actual terrestrial magmas and one can see that the H_2 flux through the melt should operate in most conditions encountered in natural magmas. Only under extremely low fH_2 and high-temperature conditions should the presence, or absence, of hydrogen in the system have no effect on the rate of redox exchange in magmas.

Communication of redox potentialin natural magmas will, according to these latest results, mainly involve H_2 transfer. At this point, we must emphasize that redox transfer can operate even when the fO_2's of two reacting bodies are similar, provided that there is an fH_2 gradient. As an example, consider two juxtaposed magmas (A and B) at 1000°C having a H_2-H_2O volatile component, which buffers a fO_2 equal to10^{-10} bar (NNO+0.34). Two magmas having the same fO_2 is unlikely but this should not affect the geological implications we draw hereafter. Furthermore, this choice was made to illustrate that redox exchange can occur even when no fO_2 gradient exists. If the water fugacities of the two magmas are dissimilar, A being equal to 1580 and B, 860 bar (~6 and 3 wt% H_2O) they will buffer an fH_2 equal to ~9 and 5 bar, respectively. It follows that H_2 transfer will operate affecting the Fe^{3+}/Fe^{2+} and therefore fO_2 of both magmas, whereas the chemical potential of O_2 was initially the same. However, in terms of rate of redox exchange between the two magmas, calculations performed by Eqns. 5 and 6 revealed that after an exposure time of 5 yr, the transfer operates only across 23 cm within magma B when a rhyolitic composition is considered (the composition of the Pinatubo glass matrix given in Gaillard et al. (2002), with FeO = 1 wt% as total iron). The implication is therefore that crustal events, such as magma mixing, or in general, interactions with surroundings, do not lead to significant modifications of the magma redox state, thus confirming the suggestions of Carmichael (1991) and Feldstein et al. (1996). This conclusion is the result of the shape under which magmas are stored in the crust (large volumes in magma chambers). Diffusion, even as

fast as H_2 diffusion, only affects the outermost zones of magmas, whereas the bulk volume remains unchanged.

Another interesting case for which our model applies is weathering of glasses used as containers for radioactive waste. Consider a glass at 200°C stored within a geological layer at a depth of 150 m in a system where free water exists ($fH_2O \sim 30$ bar). We illustrate two cases for which the redox conditions of the fluid differ: (1) the redox conditions are close to NNO + 1 so that fH_2 nearly equals 1 bar; and (2) the redox conditions affected by the presence of organic matter are slightly below the Fayalite-Magnetite-Quartz (FMQ) buffer, which is equivalent to ~10 bar of H_2. For both scenarios, H_2 will diffuse in the glass and react with the redox traps to produce OH groups at a rate controlled by both diffusion and solubility of H_2. In addition, the penetration of the redox front and the amount of reduction-derived OH are both a function of the concentration of redox traps in the glass. We symbolize the redox trap density by the Fe_2O_3 content, but other multivalent cations (manganese, uranium, sulfur…) would be equivalent, taking into account that the stoichiometry of the reaction may differ. In Figure 10, we show the rate of reduction of a glass containing 2.2 wt% of Fe_2O_3, which by interaction with H_2 will create reaction-derived OH, expressed here as equivalent H_2O (0.25 wt%). The rate of reduction is four times faster if $fH_2 = 10$ bar compared with the case where $fH_2 = 1$ bar. Compared with hydration due to molecular H_2O diffusion within the glass, the rate of OH incorporation by H_2 diffusion + reaction is 13 and 50 times faster at 1 and 10 bar fH_2, respectively. The implication is that if one ignores the possibility of H_2-iron interactions, the rate of glass hydration may be severely underestimated. For example, at $fH_2 = 1$ bar, reaction-derived OH are incorporated over 1 mm within less than 30 yr and for $fH_2 = 10$ bar, after 100 yr, 1 cm of glass becomes wet. The timescale we calculate here contrasts critically with previous estimations of rate of glass weathering, which considered that hydration of a glass is rate controlled by H_2O mobility within the glass (Grambow and Müller, 2001). As water is incorporated into a glass, its reactivity (Tg, relaxation time, leaching rates?) may be changed by several orders of magnitude (Dingwell, 1994), and it follows that the durability of the glass exposed to surroundings that contain H_2 is then questionable. Given that natural environments, where nuclear-waste-bearing glasses are stored, contain H_2 at a content controlled by the fO_2 conditions, we strongly suggest that the redox conditions in the host terrain must be one of the main parameters to be considered.

Acknowledgments—This article has benefited from the in-depth review of Prof. Fritz Seifert. F. A. Bromiley's participation to the polishing of the final version really improved the clarity of this manuscript. F.G. inherited his knowledge of redox equilibria in water-bearing melts from the experience of Michel Pichavant and Bruno Scaillet (ISTO, Orléans, France). Both are warmly thanked. This research was financed by the visitors program at the BGI. The editorial work of K. Russell and the constructive reviews of P. King, Y. Zhang, and H. Behrens were greatly appreciated.

Associate editor: F. Podosek

REFERENCES

Beckett J. R. and Mendybaev R. A. (1997) The measurement of oxygen fugacities in flowing gas mixtures at temperatures below 1200°C. *Geochim. Cosmochim. Acta* **61,** 4331–4336.

Behrens H. and Nowak M. (1997) An experimental investigation on diffusion of water in haplogranitic melts. *Contrib. Mineral. Petrol.* **126,** 365–376.

Bolfan-Casanova N., Mackwell S., Keppler H., McCammon C., and Rubie D. C. (2002) Pressure dependence of H solubility in magnesiowüstite up to 25 GPa: Implications for the storage of water in the Earth's lower mantle. *Geophys. Res. Lett.* **29,** 81–89.

Carmichael I. S. E. (1991) The redox state states of basic and silicic magmas: A reflection of their source regions. *Contrib. Mineral. Petrol.* **106,** 129–141.

Carroll M. R. and Webster J. D. (1994) Solubilities of sulfur, noble gases, nitrogen, chlorine, and fluorine in magmas. In *Volatiles in Magmas* (Carroll M. R. and Holloway J. R., eds), pp. 231–380. Reviews in Mineralogy 30. Mineralogical Society of America.

Chekhmir A. S., Persikov E. S., Epel'Baum M. B., and Bukhtiyarov P. G. (1985) Experimental investigation of the hydrogen transport through the model magmatic melt. *Geokhimya* **5,** 594–598.

Cook G. B. and Cooper R. F. (2000) Iron concentration and the physical processes of dynamic oxidation in alkaline earth aluminosilicate glass. *Am. Mineral.* **85,** 397–406.

Cooper R. F., Fanselow J. B., and Poker D. B. (1996) The mechanism of oxidation of a basaltic glass: Chemical diffusion of network-modifying cations. *Geochim. Cosmochim. Acta* **60,** 3253–3265.

Crank J. (1975) *The Mathematic of Diffusion*. 2nd ed. Oxford University Press.

Cussler E. L. (1997) *Diffusion Mass Transfer in Fluid Systems*. 2nd ed. Cambridge University Press.

Deines P., Nafziger R. H., Ulmer G. C., and Woermann E. (1974) Temperature oxygen fugacity tables for selected gas mixture in the system C-O-H at one atmosphere total pressure. Bulletin of the Earth and Mineral Sciences Station 88. Pennsylvania State University.

Dingwell D. B. (1994) Relaxation theory in silicate melts. In *Structure, Dynamics and Properties of Silicate Melts* (Carroll M. R. and Holloway J. R., eds), pp. 23–48. Reviews in Mineralogy 32. Mineralogical Society of America.

Feldstein S. N., Lange R. A., Vennemann T., and O'Neil J. R. (1996) Ferric–ferrous ratio. H_2O contents and D/H ratios of phlogopites and biotites from lavas of different tectonic regimes. *Contrib. Mineral. Petrol.* **128,** 82–92.

Gaillard F., Scaillet B., Pichavant M., and Beny J. M. (2001) The effect of water and fO_2 on the ferric–ferrous ratio of silicic melts. *Chem. Geol.* **174,** 255–273.

Gaillard F., Scaillet B., and Pichavant M. (2002) Kinetics of iron oxidation–reduction in hydrous silicic melts. *Am. Mineral.* **87,** 829–837.

Gaillard F., Pichavant M., Mackwell S. J., Champallier R., Scaillet B., and McCammon C. A. (2003) Chemical transfer during redox exchange between H_2-bearing vapor and iron-bearing melts. Am. Mineral., **88,** 308–315.

Georges P., Libourel G., and Deloule E. (2000) Experimental constraints on alkali condensation in chondrule formation. *Meteor. Planet. Sci.* **35,** 1183–1186.

Grambow B. and Müller R. (2001) First-order dissolution rate law and the role of surface layers in glass performance assessment. *J. Nucl. Mater.* **298,** 112–124.

Hess P. C. (1980) Polarization model for silicate melts. In *Physics of Magmatic Processes* (ed. R. B. Hargraves), pp. 3–48. Princeton University Press.

Holtz F., Behrens H., Dingwell D., and Johannes W. (1995) H_2O solubility in haplogranitic melts: Compositional, pressure, and temperature dependence. *Am. Mineral.* **80,** 94–108.

Ingrin J. and Skogby H. (2000) Hydrogen in nominally anhydrous upper-mantle minerals: Concentration levels and implications. *Eur. J. Mineral.* **12,** 543–570.

Johnson M. C., Anderson A. T., and Rutherford M. J. (1994) Pre-eruptive volatile contents of magmas. In *Volatiles in Magmas* (Carroll M. R. and Holloway J. R., eds), pp. 281–323. Reviews in Mineralogy 30. Mineralogical Society of America.

Knoche R., Dingwell D. B., and Weeb S. L. (1995) Leucogranitic and pegmatitic melt densities: Partial molar volumes for SiO_2, Al_2O_3, Na_2O, Rb_2O, Cs_2O, Li_2O, BaO, SrO, CaO, MgO, TiO_2, B_2O_3, P_2O_5, F_2O-1, Ta_2O_5, Nb_2O_5 and WO_3. *Geochim. Cosmochim. Acta* **59,** 22., 4645–4652.

Kress V. C. and Carmichael I. S. E. (1991) The compressibility of silicate liquids containing Fe_2O_3 and the effect of composition, temperature, oxygen fugacity and pressure on their redox states. *Contrib. Mineral. Petrol.* **108,** 82–92.

Lange R. and Carmichael I. S. E. (1990) Thermodynamic properties of silicate liquids with emphasis on density, thermal expansion and compressibility. In *Modern Methods of Igneous Petrology: Understanding Magmatic Processes*, pp. 25–64. Reviews in Mineralogy 24. Mineralogical Society of America.

Lee R. W. and Fry D. L. (1966) A comparative study of the diffusion of hydrogen in glass. *Phys. Chem. Glasses* **7,** 19–28.

Lou V., Sato R., and Tomozawa M. (2003) Hydrogen diffusion in fused silica at high temperature. *J. Noncryst. Solids* **315,** 13–19.

Martel C., Pichavant M., Holtz F., and Scaillet B. (1999) Effect of fO_2 and H_2O on andesite phase relations between 2 and 4 kbar. *J. Geophys. Res.* **104,** 453–470.

McCammon C. A. (1994) A Mössbauer milliprobe: Practical considerations. *Hyperfine Interactions* **92,** 1235–1239.

McCammon C. A., Chaskar V., and Richards G. G. (1991) A technique for spatially resolved Mössbauer spectroscopy applied to quenched metallurgical slags. *Measurement Sci. Technol.* **2,** 657–662.

Mysen B. O., Virgo D., Newman E. R., and Seifert F. A. (1985) Redox equilibria and structural position of ferric and ferrous iron in melts in the system CaO-MgO-Al_2O_3-SiO_2-Fe-O: Relationships between redox equilibria, melt structure, and liquidus phase equilibria. *Am. Mineral.* **70,** 487–498.

Newman S., Stolper E. M., and Epstein S. (1986) Measurement of water in rhyolitic glasses: Calibration of an infrared spectroscopic technique. *Am. Mineral.* **71,** 1521–1527.

Osborn E. F. (1959) Role of oxygen pressure in the crystallization and differentiation of basaltic magma. *Am. J. Sci.* **257,** 609–647.

Persikov E. S., Zharikov V. A., Bukhtiyarov P. G., and Pol'skoy S. F. (1990) The effect of volatiles on the properties of magmatic melts. *Eur. J. Mineral.* **2,** 621–642.

Pichavant M., Mysen B. O., and MacDonald R. (2002) Source and H_2O content of high-MgO magmas in island arc settings: An experimental study of a primitive calc-alkaline basalt from St. Vincent, lesser Antilles arc. *Geochim. Cosmochim. Acta* **66,** 2193–2209.

Schmidt B. C., Scaillet B., and Holtz F. M. (1995) Accurate control of fH_2 in cold-seal pressure vessels with the Shaw membrane technique. *Eur. J. Mineral.* **7,** 893–903.

Schmidt B. C., Holtz F. M., and Beny J.-M. (1998) Incorporation of H_2 in vitreous silica, qualitative and quantitative determination from Raman and infrared spectroscopy. *J. Noncryst. Solids* **240,** 91–103.

Watson E. B. (1994) Diffusion in volatile-bearing magmas. In *Volatiles in Magmas* (Carroll M. R. and Holloway J. R., eds), pp. 371–411. Reviews in Mineralogy 30. Mineralogical Society of America.

Zhang Y., Stolper E. M., and Wasserburg G. J. (1991) Diffusion of water in rhyolitic glasses. *Geochim. Cosmochim. Acta* **55,** 441–456.